fibers

MDPI

Article

Experimental and Numerical Investigation of the Impact Resistance of Synthetic Fiber-Reinforced UHPC Thin Panels

Vincenzo Romanazzi [1,*], Francesco Micelli [1], Sandro Moro [2], Pedro Serna Ros [3] and Maria Antonietta Aiello [1]

[1] Department of Engineering for Innovation, University of Salento, 73100 Lecce, Italy; francesco.micelli@unisalento.it (F.M.); antonietta.aiello@unisalento.it (M.A.A.)
[2] Master Builders Solutions, 31100 Treviso, Italy; sandro.moro@masterbuilders.com
[3] Instituto de Ciencia y Tecnología Del Hormigòn (ICITECH), Universitat Politecnica de Valencia, 46022 Valencia, Spain; pserna@cst.upv.es
* Correspondence: vincenzo.romanazzi@unisalento.it; Tel.: +39-3929065876

Highlights

What are the main findings?

- Drop-weight impact tests on thin VHPC panels showed that synthetic fiber reinforcement significantly improves impact resistance: PVA microfibers reduced crack openings by more than 20 times compared to plain VHPC, while PP macrofibers were less effective at the tested energy level due to their greater efficiency at larger crack openings.
- A finite element model based on the fib Model Code 2010 inverse analysis and the Concrete Damaged Plasticity framework accurately reproduced the experimental crack patterns and deflections of all fiber-reinforced panels.

What are the implications of the main findings?

- At low-to-medium impact energy levels, PVA microfibers provide the dominant contribution to impact resistance in thin VHPC panels, suggesting that fiber selection should account for the expected crack opening range under the design impact scenario.
- The proposed numerical approach, calibrated on quasi-static bending tests, proves adequate for predicting the impact response of thin VHPC panels, offering a reliable and practical tool for structural design.

Abstract

In recent years, Ultra High-Performance Fiber-Reinforced Concretes (UHPFRCs) have gained significant attention for their applications in structural components, particularly for improving impact resistance and post-cracking behavior. This study explores the behavior of thin Ultra High-Performance Concrete (UHPC) panels reinforced with synthetic fibers, focusing on the potential use of these materials for building façades. Three different synthetic fiber-reinforced mixes were developed, utilizing polyvinyl alcohol (PVA) microfibers, polypropylene (PP) macrofibers, and a hybrid combination of both. These thin, unreinforced panels were subjected to impact testing using a free-falling steel ball to evaluate their mechanical response. The results were analyzed in terms of crack patterns, crack openings, and overall impact resistance. Additionally, numerical analysis was implemented by using the ABAQUS^{TM} finite element code, in order to predict the panels' performance under impact, providing a comparison between experimental results and numerical simulations. This investigation highlights the significant contribution of synthetic fibers in enhancing the toughness and impact resistance of UHPC panels, demonstrating their viability for structural applications requiring enhanced durability.

Check for updates

Academic Editors: Theodoros Rousakis, Ioannis E. Kavvadias, Maria C. C. Naoum, Kosmas E. Bantilas and Emmanouil Golias

Received: 19 February 2026
Revised: 11 May 2026
Accepted: 15 May 2026
Published: 19 May 2026

Copyright: © 2026 by the authors. Licensee MDPI, Basel, Switzerland. This article is an open access article distributed under the terms and conditions of the Creative Commons Attribution (CC BY) license.

Keywords: ultra high-performance fiber-reinforced concrete; synthetic fibers; polyvinyl alcohol fibers; polypropylene fibers; impact test; FEM simulations

1. Introduction

Concrete remains the most widely used construction material worldwide due to its high compressive strength and high workability that makes it suitable for a very wide range of design situations. In recent decades, novel classes of cementitious materials such Ultra-High-Performance Concrete (UHPC, f_c higher than 120 MPa) have been developed, in order to reach enhanced compressive strength, reduced porosity, and improved durability compared to conventional concretes [1–3].

Despite significant increases in mechanical performance, the inadequate energy absorption and post-cracking ductility of conventional concrete under dynamic loading may be still a limit to overcome extreme load conditions [4]. In recent decades, the frequency and intensity of accidental and deliberate dynamic loading events affecting concrete structures has increased significantly, driven by factors such as urban densification, transportation accidents, and security threats [5–8]. To address the limitations of plain concrete when subjected to impacts and explosions, several studies [7,9] have proposed reinforcing methods such as continuous textile layers, randomly distributed short fibers, or strengthening methods by using externally bonded fiber-reinforced polymer (FRP) systems. Among these techniques, the incorporation of short discontinuous fibers—made from materials like steel, polymer, carbon, or basalt—has been the most widely adopted [10], as they can be easily mixed into concrete, effectively enhance its toughness under impact or blast through fiber bridging, and provide a more cost-effective solution compared to other reinforcement methods [11]. The durability in terms of reduced crack opening under static loads is also increased [12,13]. In addition, both steel and PP fibers have been demonstrated to play a beneficial role under fire exposure [14]. PP fibers melt at relatively low temperatures (approximately 160 °C), creating additional porosity that facilitates the release of internal pore pressure and significantly reduces the risk of explosive spalling [15,16], which is a particularly critical failure mode for high-strength and high-performance concrete. On the other hand, steel fibers can enhance strength of concrete during fires due to its strong thermal stability, resulting in fewer cracks [17].

Starting from the earliest studies to the most recent applications, the random distribution of steel fibers within the concrete matrix has been shown to clearly influence the material's mechanical performance. Specifically, steel fibers help to control the initiation and propagation of cracks, thereby enhancing the tensile, flexural, and impact strength as well as the overall toughness of concrete [18,19]. On the other hand, exposure to aggressive chloride environments can damage the protective film on steel fibers, leading to corrosion and reduced concrete durability [20]. Research has shown that both pitting and uniform corrosion significantly decrease the tensile strength of steel fibers, with pitting often causing brittle failure [21,22], ultimately compromising the mechanical performance of steel fiber-reinforced concrete [23].

Synthetic fibers have proven to be a great alternative, able to offer enhanced crack control, improved toughness [24], and superior resistance to chemical degradation, thus overcoming the durability issues typically associated with steel fibers [25]. In fact, they may be used to improve concrete performance in a cost-effective and sustainable manner. A wide range of polymeric fibers has been successfully incorporated into cementitious composites through the years, including polyethylene (PE), polyvinyl alcohol (PVA),

polypropylene (PP), polyamide (PA), aramid, polyacrylonitrile (PAN), polyester (PES), and carbon fibers [26].

Among synthetic fibers, polypropylene (PP) has gained particular interest due to its ability to maintain mechanical performance even when exposed to aggressive environments, where steel fibers tend to suffer corrosion-induced degradation. PP fibers are commercially available in a wide range of shapes and surface textures, such as straight, embossed, and crimped profiles, which are specifically engineered to enhance mechanical interlock with the cementitious matrix [27]. These geometrical modifications play a crucial role in improving pull-out resistance and increasing the post-cracking energy absorption capacity of concrete [28,29]. From a mechanical point of view, PP fibers typically exhibit tensile strengths up to 900 MPa and elastic moduli within the range characteristic of polymer-based reinforcements, making them effective in mitigating crack propagation under tensile and impact loading. Several experimental studies have shown that the inclusion of PP macro-fibers does not adversely influence compressive strength and, in some cases, leads to slight improvements, depending on fiber dosage and matrix composition [30,31]. Additionally, PP fibers have been reported to influence the permeability of concrete in two contrasting ways. On one hand, non-uniform fiber distribution may induce voids in the concrete matrix, potentially increasing water permeability in the uncracked material [32]. On the other hand, fiber bridging limits the opening of micro-cracks, reducing the pathways available for aggressive agents to penetrate the cracked material; a reduction in cracked area of 65% with 0.07% PP fiber content was associated with a 24.3% decrease in average water penetration depth [33]. The net effect on permeability therefore depends on fiber dosage, distribution, and the extent of cracking experienced by the element [13], contributing to the long-term durability of concrete structures exposed to aggressive environments when crack control is effective [13,34].

As previously introduced, impact resistance represents another crucial aspect of fiber reinforcement, especially for thin structural or precast elements. As defined in [35], there are four categories in which the existing high-rate strain test system can be divided: (1) potential-energy-based, in which a relatively heavy mass is released by falling or swinging from a defined height to strike the specimen at low velocity, as in Charpy, Izod, and drop-weight setups [36,37]; (2) kinetic-energy-based, in which a lighter projectile is accelerated to high speed, typically using a gas-gun arrangement, and then directed onto the specimen [38,39]; (3) hydraulic-machine-based, in which hydraulic actuators are employed to impose deformation on the sample at intermediate loading velocities [40]; and (4) stress-wave-propagation-based, where a stress wave is generated and transmitted through an elongated bar before reaching and loading the specimen [8,8]. Drop-weight tests are the most common for structural elements: they are simple to set up and allow good control of impact energy, but are limited to low-to-medium velocity ranges [41]. Projectile and ballistic impact tests replicate high-velocity scenarios and are used for protective structures, though they require complex equipment and strict safety measures [42]. Split Hopkinson pressure bar (SHPB) tests are suitable for material characterization at high strain rates, but are restricted to small specimens and cannot reproduce structural-scale behavior [43]. Charpy and pendulum tests are standardized and widely used to assess fracture toughness, but apply mainly to notched specimens and are less representative of real impact events on structural elements [44].

The drop-weight impact technique allows evaluating the specimen's flexural and compressive behaviors [36,45]. This setup applies an impact at midspan by dropping a mass from a selected height, which governs the input energy. Assuming negligible friction between the hammer and its guide, the corresponding impact velocity can be derived from the energy balance $E = \frac{1}{2}mv^2$, where m is the hammer mass and v the velocity at impact.

The impact resistance of concrete is strongly influenced by matrix compressive and tensile strength [46–50]. Higher strength improves resistance to crack initiation and increases energy absorption. Drop-weight tests show that impact resistance grows with both compressive strength and fiber dosage [46]. Tests on high-strength concrete confirm that higher strength reduces crack development and improves energy dissipation [48,50]. UHPC achieves superior impact resistance due to its dense microstructure and fiber bridging, with fracture energy above 2000 N/m when steel fibers are used [49]. Tensile strength also governs the fracture mode: lower values produce tensile cracks, while higher values lead to shear-type failure [47].

It is well established that the mechanical properties of fiber-reinforced concrete are strain-rate dependent. Experimental studies on steel fiber-reinforced concrete have reported considerable increases in tensile strength, strain at maximum stress, and fracture energy with increasing loading rate [51]. For high-performance fiber-reinforced cementitious composites (HPFRCC), dynamic increase factors (DIF) for first-cracking and post-cracking strength up to 2.0 and 1.7, respectively, have been reported depending on fiber type and volume fraction [40]. The response of UHP-FRC under varying strain rates has been investigated by Fujikake et al. [52], who proposed a rate-dependent bridging law relating tensile stress to crack opening, and by Wille et al. [53], who observed that both strength and energy absorption capacity increase with fiber volume fraction at a given strain rate. More recently, Pyo et al. [54] reported that for UHP-FRC the DIF for post-cracking strength and energy absorption capacity increase log-linearly with strain rate, reaching approximately 1.3 and 2.0 at seismic rates (0.1 s^{-1}), respectively. Notably, unlike conventional HPFRCC, the strain capacity of UHP-FRC was found not to decrease with increasing strain rate. Under drop-weight impact loading, strain rates are typically higher than the seismic range, implying that the actual dynamic response of the material would be at least as favorable as quasi-static predictions.

Several studies have compared the contributions of different fiber types to the impact performance of concrete. At low fiber dosages (up to about 0.5%), hooked-end steel fibers have been shown to enhance the fracture energy of concrete beams under impact more effectively than PP fibers. In [36], it has been observed that steel fibers provided the most significant improvement in toughness for wet-mix shotcrete elements, under both static and dynamic loading, in respect to PP and PVA fibers. When comparing polymeric fibers, Ref. [36] reported PP fibers generally offered higher impact resistance than PVA. In the same way, Refs. [55,56] further demonstrated that macro steel fibers deliver substantially greater resistance to crack propagation than micro-PP fibers under either static or impact loading conditions.

On the other hand, Refs. [55,57] report that the gap between steel and polymeric fibers reduces as the impact load increases. Although deformed steel fibers generally produce much higher energy absorption than synthetic fibers in flexural tests, the relative difference is lower under higher energy impact loading. In fact, long PP fibers were able to dissipate about 80% of the energy absorbed by steel fibers under impact. Based on these observations, the authors concluded that appropriately designed PP fibers, considering length, shape, and surface deformation, can reach similar levels of fracture-energy absorption as deformed steel fibers. At even higher impact energies (impact energy around 600 J), ultra high-performance concretes reinforced with crimped PP fibers were found to exceed the flexural toughness of those reinforced with flat-end steel fibers [58]. This trend was attributed to the enhanced elastic response of the PP fibers under high-rate loading.

2. Materials and Methods

2.1. Methodology

In this paper, the impact resistance of UHPC reinforced with different types of synthetic fibers has been investigated. Three fiber-reinforced mixes and a plain UHPC mix have been tested under drop-weight impact loading. A complete and detailed overview of the mechanical characteristics of these UHPC mixes, including compression strength, elastic modulus and toughness, according to both EN 14651 [59] and ASTM 1609 [60], has been reported in [61]. In particular, the fiber-reinforced UHPC mixes (UHPFRC) were realized with these types of fibers: one with PVA microfibers, one with PP macrofibers, and one hybrid combination of the two previous types. Their performance under drop-weight impact loading was compared with that of plain UHPC panels, and the results were validated against finite element simulations. The outcomes provide new insights into the role of synthetic fibers in enhancing toughness, crack control, and energy absorption in thin UHPFRC elements, highlighting their potential for precast façade applications where durability and impact resistance are critical design issues.

2.2. Materials

Three different types of synthetic fibers have been used in this research activity, as shown in Table 1. These fibers were chosen for their potential to improve impact resistance and toughness of the concrete panels as defined in [61].

Table 1. Fibers properties according to manufacturer technical data sheet.

Fiber Name	Material	Length [mm]	Equivalent Diameter [mm]	Aspect Ratio	Shape	Tensile Strength [MPa]	Elastic Modulus [MPa]
MasterFiber 401	Polyvinyl alcohol	12	0.20	60	straight	800	27,000
MasterFiber 236	Polypropylene	29	0.75	38.6	waved	450	3250
MasterFiber 246	Polypropylene	40	0.75	53.3	waved	450	3250

- PVA Microfibers (MasterFiber 401): These 12 mm-long fibers with a diameter of 0.2 mm were selected for their ability to control crack formation, particularly in reducing shrinkage cracks.
- PP Macrofibers (MasterFiber 236 and 246): These fibers, 30 mm and 40 mm in length, respectively, have a waved shape, which enhances their bond with the concrete matrix, thereby improving toughness and ductility under impact loads.

The experimental investigation involved the four UHPC mixtures described and tested in [61], one of which served as a control mix without any fiber reinforcement, while the other three were reinforced with different synthetic fibers. The control mix consisted of cement, silica fume, fine, medium, and coarse sands, water, and superplasticizer, as shown in Table 2. Two different fibers length were used since it is expected, from the studies under monotonic static loads [30], that the propagation of the crack is sensitive, at different stages, to fibers dispersion and length.

Table 2. UHPFRC mix design used and characterized in [61].

Components	Quantity [kg/m^3]			
	UHPC	UHPFRC_1	UHPFRC_2	UHPFRC_3
Fine Sand (<0.5)	305	305	305	305
Medium Sand (0.6 < d < 1.2)	365	365	365	365
Coarse Sand (>1.2)	225	225	225	225

Table 2. *Cont.*

Components	Quantity [kg/m^3]			
	UHPC	**UHPFRC_1**	**UHPFRC_2**	**UHPFRC_3**
Silica fume	175	175	175	175
Cement	800	800	800	800
Water	170	170	170	170
Superplasticizer	31.8	31.8	31.8	31.8
MF401	-	30	-	20
MF236	-	-	30	-
MF246	-	-	-	10

2.3. Mechanical Properties of UHPFRC

As previously reported, the outcome of the experimental activity regarding the mechanical characterization of these mixes is shown and deeply discussed in [61]. The three-point bending tests were carried out on prismatic notched beams with dimensions of 150 × 150 × 600 mm^3 (width × height × length), with a notch of 25 mm depth cut at mid-span, in accordance with UNI EN 14651 [59]. In particular, the crack mouth opening displacement (CMOD) has been measured by means of a linear variable displacement transducer (LVDT) positioned below the notch of the beam. As suggested by the standard, the results of these tests are given as flexural strength vs. CMOD graphs. The average results obtained from compression tests on five cubic specimens, elastic modulus tests on three cylinders, and the three-point bending tests are shown in Table 3. The results of the bending tests are expressed in terms of limit of proportionality (LOP) stress and the flexural stresses f_{rj} corresponding to the $CMOD_j$ values (j = 1, 2, 3, 4). Regarding the toughness results (Figure 1), it can be seen that the first linear elastic stage is the same for the three mixes in terms of both the LOP and the slope of the initial branch. Once the crack occurred, it is evident how the PVA microfibers allowed better control of the load decay and faster recovery of the load than the other mixes. Finally, the evident differences in the post-cracking behavior for high values of crack opening mount can be seen. The PP macrofibers included in mix UHPFRC_2 allowed the specimens to carry a higher load from CMOD equal to 1 mm to the end of the tests. On the other hand, the mix UHPFRC_3, realized with both PVA microfibers and PP macrofibers, seemed to stay in the middle between the other two UHPFRC mixes. Despite the fact that the contribution of the PVA microfibers appeared not so evident in this mix, since no significant differences are seen for low CMOD values, the influence of MF246 can be noted for a larger CMOD when the curve is compared with the one of UHPFRC_1.

Table 3. Compressive strength R_c, elastic modulus E and CMOD from three-point bending tests on notched beams (CoV values in parentheses) [61].

MIX	Properties from Compression			Properties from Three Point Bending Test				
	R_c [MPa]	E [MPa]	LOP [MPa]	CMOD 0.5 mm	CMOD 1.5 mm	CMOD 2.5 mm	CMOD 3.5 mm	f_{r3}/f_{r1} [-]
				f_{r1} [MPa]	f_{r2} [MPa]	f_{r3} [MPa]	f_{r4} [MPa]	
UHPC	121.39 (4.1%)	44234 (0.9%)	6.71 (2.8%)	-	-	-	-	-
UHPFRC_1	119.9 (6.0%)	41452	6.77 (2.4%)	6.77 (3.8%)	4.38 (7.5%)	2.03 (10.2%)	1.11 (10.9%)	0.30
UHPFRC_2	108.4 (1.2%)	40407 (2.1%)	6.54 (4.0%)	5.83 (11.0%)	7.97 (11.5%)	8.43 (12.8%)	8.13 (13.2%)	1.45
UHPFRC_3	111.0 (2.7%)	42306 (2.0%)	7.04 (4.8%)	5.97 (20.8%)	5.82 (24.0%)	4.87 (24.4%)	4.63 (31.6%)	0.82

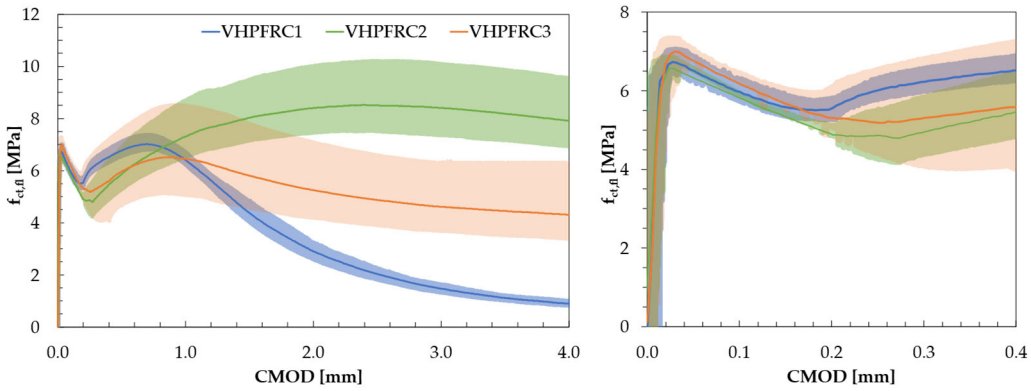


Figure 1. Average curves of three-point bending results on UHPFRC mixes [61] and zoomed inset of the initial CMOD region.

3. Impact Tests

3.1. Tests Setup

The primary objective of the impact tests conducted and described in this study was to compare the reference mix without fibers to three different UHPFRC mixes, assessing the effects of various fiber types and their combination. Additionally, the results obtained were used to validate a numerical model, which could later be applied for quantitative analysis in specific cases.

Four thin, unreinforced panels—one for each mix—were cast using the three UHPFRC mixes and the previously described reference UHPC mix. Each panel had a square surface with a side length of 1000 mm and a thickness of 40 mm. The test setup, illustrated in Figure 2, involved dropping a steel ball with a diameter of 120 mm and a weight of 7.7 kg from a height of 1000 mm onto the center of the panels. The panels were supported along all four edges by steel beams, as shown in Figure 2. The panels rested on the beams over a contact width of a few centimeters, with no mechanical fastening. This configuration closely approximates simply supported boundary conditions, allowing free rotation at the edges. The ball was suspended from a horizontal rod by a rope, which was cut to initiate the test.

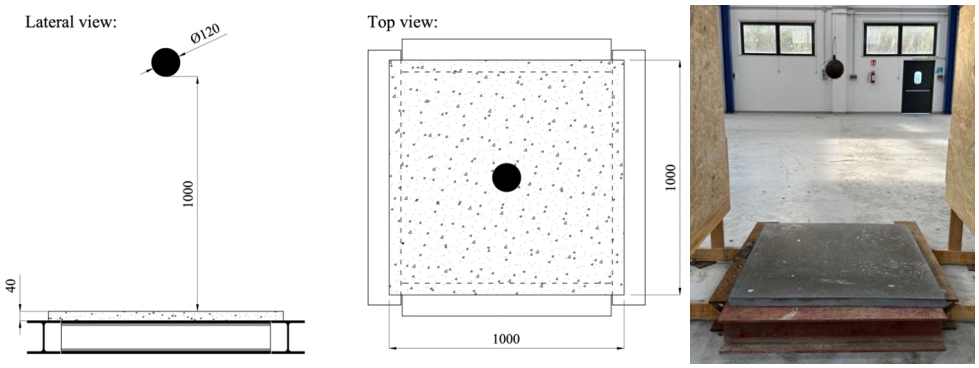


Figure 2. Impact tests setup (dimensions in mm).

The central deflection at the moment of impact was estimated by means of scaled digital photo analysis of images captured during the test. A reference scale was placed adjacent to the panel, and the deflection of the panel center was measured from the photographic record. This approach was adopted due to the absence of contact sensors at the impact location, which could interfere with the free-fall trajectory of the steel ball. In addiction, after each test, the crack width has been measured using a Dino-Lite digital microscope(AnMo Electronics Corporation, New Taipei City, Taiwan). The drop height

of 1000 mm was set by fixing the release point of the steel ball at a measured and marked position above the panel surface, verified before each test with a graduated measuring tape. The ball was centered over the panel by means of a laser pointer, ensuring that the impact point coincided with the geometric center of the upper surface. The same setup, drop height, and steel ball were used for all tests to guarantee consistent conditions across the four panels.

Since in this case it was not possible to measure the peak impact force, the following procedure has been used in order to calculate the average impact force for each test (i.e., average over distance impact force). Generally, it is considered that the average impact force corresponds to half the peak force during impact. In particular, this process is based on the work-energy principle according to whom the change in the kinetic energy of an object is equal to the net work (W_{net}), in terms of kinetic energy, done on the object:

$$W_{net} = \frac{1}{2}mv_f^2 - \frac{1}{2}mv_i^2$$

where m is the mass, the final velocity v_f is equal to zero after the impact and the initial velocity v_i is the velocity of the ball right after the impact. For straight-line impact, the net work can be calculated as the average force of impact (F_{avg}) multiplied for the distance traveled by the object during the impact:

$$W_{net} = F_{avg} \cdot x$$

in such case, the distance x covered by the object during the impact corresponds to the deflection of the panel measured in the impact point (i.e., the central point of the panel). Firstly, the application of the conservation energy to a falling object allows easily predicting its impact velocity and the kinetic energy. In fact, the impact velocity can be obtained by means of the equation:

$$v = \sqrt{2gh}$$

where g is the gravity acceleration and h is the height from which the ball was dropped. In this case the impact velocity resulted to be equal to 4.43 m/s and allow calculating the kinetic energy at the impact as:

$$K = \frac{1}{2}mv^2$$

where m is the weight of the steel ball. For these tests, the ball had a kinetic energy of 75.5 J at the instant before impact. In practice, the steel ball may not come to a complete stop and could rebound producing secondary impacts. However, for the purpose of calculating the average impact force, the final velocity v_e is conservatively assumed to be zero, so that the total kinetic energy equals the net work transferred to the panel. This assumption is consistent with the experimental observations: for all tested panels, the rebound of the steel ball after impact was negligible, with the ball coming to a near-complete stop at the panel surface. Under this condition, the kinetic energy at impact is entirely transferred to the panel, and the assumption does not introduce a significant error in the average force calculation. The average impact force can then be calculated as:

$$F_{avg} = W_{net}/x$$

where x is considered as the central point panel deflection.

3.2. Results

The first panel subjected to the drop-weight impact test was the plain concrete one, without any fiber reinforcement. Figure 3 shows the crack mapping on the upper and

lower surface of each panel. In the case of the UHPC panel (Figure 3a), upon impact, a prominent crack suddenly formed, as clearly visible in the images, extending from the point of impact to one edge of the panel. In this case, as well as for the other panels tested, no perforation of the panel by the steel ball was detected. The rebound of the steel ball after impact was monitored for all tested panels. In all cases, the rebound was negligible: the ball came to a near-complete stop at the panel surface, with no appreciable secondary impact detected. This behavior indicates that the panels effectively dissipated the kinetic energy of the impactor through crack formation, fiber bridging, and inelastic deformation, with minimal elastic energy returned to the ball.

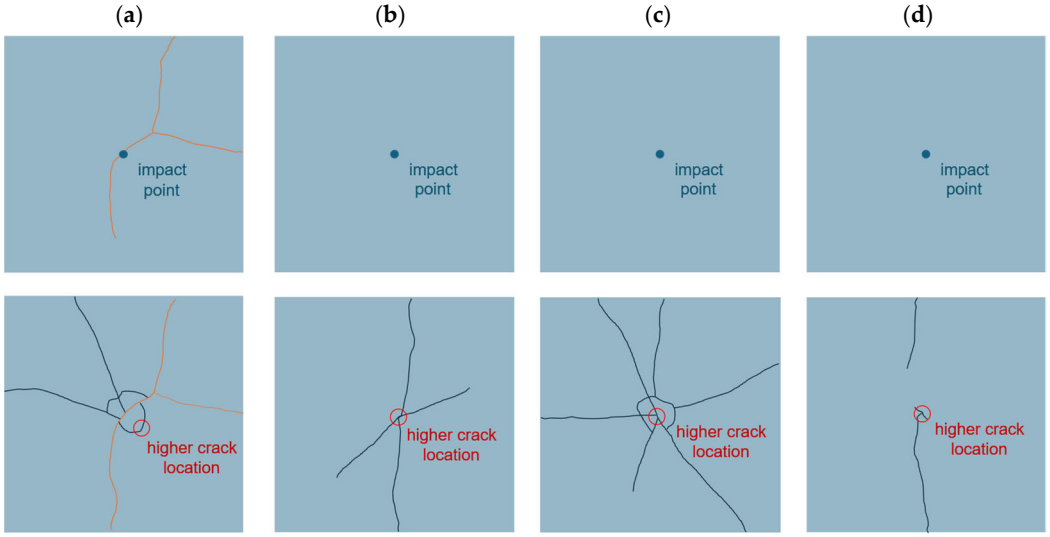


Figure 3. Crack mapping on the upper and lower surface (orange line for through-cracks) of: (**a**) UHPC; (**b**) UHPFRC_1; (**c**) UHPFRC_2; and (**d**) UHPFRC_3.

The maximum crack opening measured on the UHPC specimen was 3.87 mm, located at the center of the lower panel surface. Additionally, as shown in Table 4, the deflection at the panel's central point, determined through scaled digital photo analysis, was 6.4 mm.

Table 4. Impact test results.

Mix	Higher Crack Opening [mm]	Central Point Deflection [mm]	Average Impact Force [kN]
UHPC	3.87	6.4	11.8
UHPFRC_1	0.19	2.4	31.5
UHPFRC_2	0.46	3.2	23.6
UHPFRC_3	0.19	2.2	34.3

The impact effects on the UHPFRC_1 panel are illustrated in Figure 3b. The top surface of the panel showed no significant damage from the steel ball impact. Apart from a small, localized crack at the point of impact, no additional cracks were detected across the surface. In contrast, damage to the lower surface was considerably reduced compared to the plain UHPC panel. As seen in Figure 3b, only two cracks formed after impact. The maximum crack opening measured was 0.19 mm—more than an order of magnitude smaller than that observed in the UHPC panel. This indicates that the PVA microfibers (MF 401) played a crucial role in minimizing the damage propagation inside the panel.

The images in Figure 3c illustrate the impact test results for the UHPFRC_2 panel. Similar to the UHPFRC_1 panel, no through-cracks were observed in this case. The crack

pattern on the lower surface is shown in Figure 3c. Although a circular perimeter crack was observed on the lower surface of the UHPFRC_2 panel, no cracks were detected on the upper surface. This crack pattern is consistent with a flexural failure mode, in which tensile cracks develop on the bottom face without propagating through the full panel thickness. No through-thickness cracking was detected.

The maximum crack opening measured was slightly larger than that of the UHPFRC_1 panel, reaching 0.46 mm. This finding is supported by the bending characterization reported in Table 3 [48]. PVA microfibers (MF401, 12 mm) possess superior mechanical properties—tensile strength 800 MPa and elastic modulus 27 GPa—compared to PP macrofibers (MF236, 30 mm: 450 MPa and 3.25 GPa). These properties make PVA fibers more efficient in bridging micro-cracks at small crack openings (CMOD up to approximately 1.2 mm). At larger crack openings, PP macrofibers become progressively more effective: their greater length allows sustained load transfer across wider crack faces. Specifically, Table 3 reports residual flexural strengths of f_{R1} = 6.77 MPa at CMOD = 0.5 mm for UHPFRC_1 (PVA) and 5.83 MPa for UHPFRC_2 (PP), confirming the superior bridging efficiency of PVA at early crack opening stages. The crack openings measured under impact are consistent with this behavior.

For the panel incorporating both PVA microfibers and PP macrofibers (MF 246), the resulting crack pattern is shown in Figure 3d. Notably, the damage closely resembled that observed in the UHPFRC_1 panel, primarily due to the reinforcing effect of the PVA microfibers. As seen in Figure 3d, only two cracks formed, with the maximum crack opening measuring 0.19 mm.

The addition of synthetic fibers significantly improved the impact response of thin UHPC panels. As shown in Table 4 and Figure 3, all fiber-reinforced mixes outperformed the plain UHPC panel. The UHPFRC_3 hybrid mix (PVA + PP) achieved the highest average impact force (34.3 kN) and the lowest central deflection (2.2 mm), followed by UHPFRC_1 (PVA only, 31.5 kN, 2.4 mm) and UHPFRC_2 (PP only, 23.6 kN, 3.2 mm). The plain UHPC panel recorded the lowest values (11.8 kN, 6.4 mm). In terms of crack control, PVA microfibers proved more effective than PP macrofibers for this application, as confirmed by the comparison between UHPFRC_1 and UHPFRC_2: PVA fibers reduced crack number, length, and opening during the formation and propagation stages. The results in Table 4 show that UHPFRC_1 and UHPFRC_3 achieved similar impact performance, with differences within the range of experimental scatter. This suggests that, at the tested energy level, PVA microfibers provide the dominant contribution to impact resistance, owing to their effectiveness at controlling crack initiation and bridging at small crack openings. PP macrofibers, which are more effective at larger openings, are expected to become more influential at higher impact energies, where crack propagation extends over a wider range of opening widths [61]. For this purpose, the addition of PP macrofibers in UHPFRC_3 does not produce a systematic improvement at this scale.

4. Numerical Analysis

In order to implement the mechanical properties of the tested UHPFRC into a numerical code able to run a finite element analysis (FEA), an inverse analysis has been performed priorly by means of the experimental data obtained from three-point bending tests [62]. In this case, the inverse analysis has been conducted by following the indications reported in the fib Model Code 2010 (MC 2010) [2] section dedicated to fiber-reinforced concrete as shown in Figure 4.

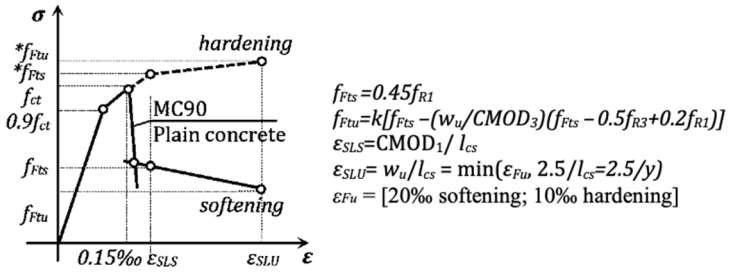


Figure 4. Direct approach inverse analysis according to Model Code 2010 [2].

The parameters used in the inverse analysis illustrated in Figure 4 are defined as follows: f_{ct} is the concrete tension strength, here determined with the formulationIn Proceedings of the $f_{ct} = 2,12 \cdot ln(1 + (f_c/10))$ purposed by Eurocode 2 [3]; f_{Fts} is the serviceability residual strength; f_{Ftu} is the ultimate residual strength; w_u is the maximum crack opening accepted for structural design, considered equal to 2.5 mm; ε_{SLS} and ε_{SLU} represent the strain at the serviceability and ultimate limit state respectively; l_{cs} is the structural characteristic length, assumed equal to the height of the specimen above the notch h_{sp} (as defined in [59]), which for elements without traditional reinforcement under bending corresponds to the height of the resisting cross-section; and ε_{Fu} is the ultimate strain. The inverse analysis yields a stress–strain relationship in which crack opening and strain are linked through lcs as $w = \varepsilon \times l_{cs}$. In the finite element model, l_{cs} was set equal to the element size in the impact zone (10 mm), so that the fracture energy dissipated per unit crack area remains independent of mesh refinement, consistently with the crack band approach.

Based on the experimental results obtained from the three-point bending tests (Figure 1), it has been considered a tensile stress–strain softening behavior for the mixes UHPFRC_1 and UHPFRC_3 and a hardening branch in the case of UHPFRC_2 mix.

A calibration phase was subsequently performed in order to ensure consistency between the experimental impact results and the numerical response of the panels. The calibration involved minor adjustments of the post-cracking parameters within the range of experimental variability observed in the bending tests. This step was considered necessary to account for the specific behavior of UHPC reinforced with synthetic fibers, whose crack-bridging mechanisms differ from those typically associated with steel fiber-reinforced concrete, for which the inverse analysis procedure was originally formulated.

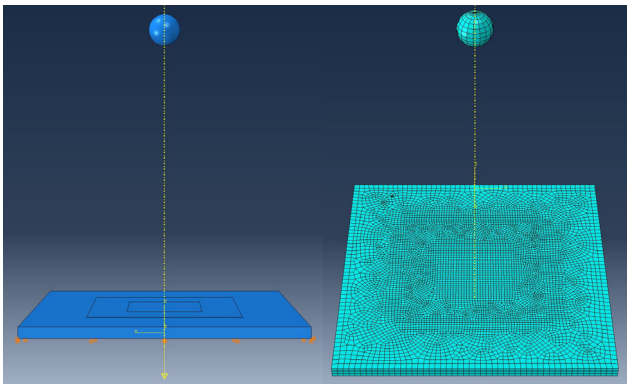
The calibrated model showed good agreement with the laboratory results in terms of crack opening and deflection, confirming the reliability of the adopted approach.

4.1. Simulations Setup and Input Parameters

The simulated impact test on ABAQUS™ (Dassault Systèmes Simulia Corp., Providence, USA) reproduced the same conditions as the laboratory tests. The panel dimensions were 1000 × 1000 mm^2 with 40 mm thickness. The ball had 120 mm diameter and weighed 7.7 kg; it was released from rest at 1 m above the panel, with gravity applied throughout the analysis. Supports were modeled as boundary strips along all four panel edges, with the same width as the actual contact area and simple support constraints, as can be seen from Figure 5a. The compressive behavior was modeled using a parabolic stress–strain law [2], with the compressive strength values from Table 3 as input. Cracking was simulated with the Concrete Damaged Plasticity (CDP) model. The steel ball was modeled as an elastic body (E = 210 GPa, ν = 0.3), with a general contact interaction at the ball-panel interface. Table 5 reports the main parameters used in the finite element model. A mesh size of 10 mm was used in the impact zone and 20 mm in the outer regions (Figure 5b); a mesh convergence study confirmed that results from the 10 mm and 5 mm meshes differ by less than 3%. Apart from the tensile post-cracking behavior defined by inverse analysis, five

additional parameters required by the CDP model were set based on values commonly adopted for UHPC [63–65]:

- Dilation angle ψ in the p-q plane, in which p corresponds to the hydrostatic stress state and q represents the Von-Mises criterion, considered equal to 31°;
- Flow potential eccentricity ϵ considered equal to 0.1;
- The ratio f_{b0} / f_{c0} of biaxial compressive yield stress to uniaxial compressive yield stress considered equal to 1.16;
- The ratio K of the second stress invariant on the tensile meridian to that on the compressive meridian for the yield function considered equal to 2/3;
- The viscosity parameter μ (relaxation time) considered equal to 0.



(**a**) (**b**)

Figure 5. Finite element model: (**a**) support and gravity load; (**b**) elements mesh.

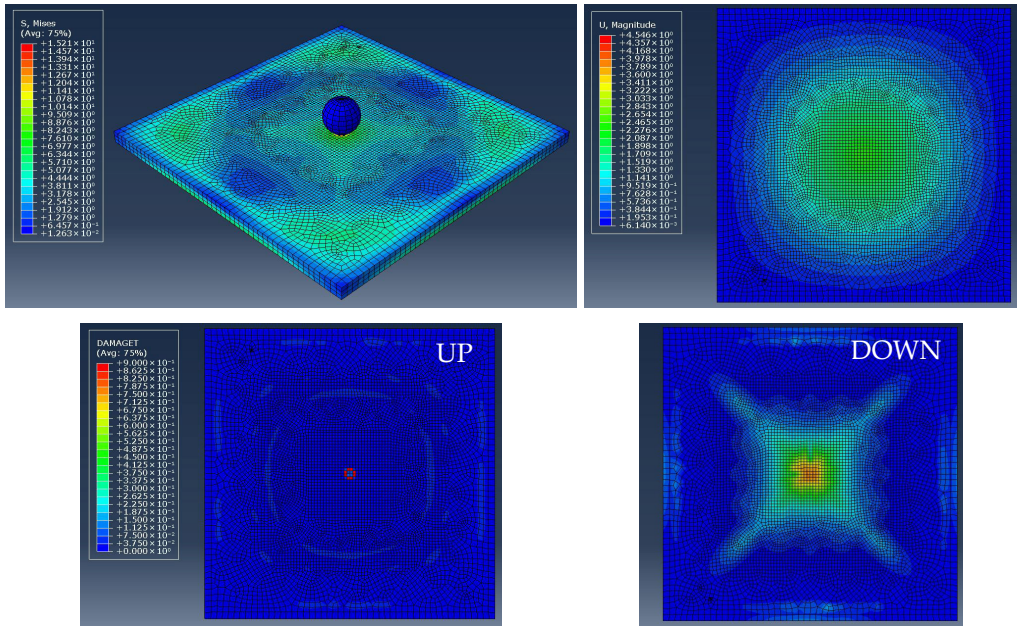
Table 5. Summary of finite element model parameters.

Parameter	Value/Description
Software	ABAQUS™/Explicit v.2022
Crack model	Concrete Damaged Plasticity (CDP)
Panel element type	Hex elements, structured technique
Steel ball element type	Hex-dominated elements, sweep technique
Mesh size (panel-impact zone)	10 mm
Mesh size (panel-edges)	20 mm
Mesh size (steel ball)	5 mm
Contact formulation	General “hard” contact, friction coefficient = 0.2
Buondary conditions	Simply supported on four edges (pinned)
Gravity	Included

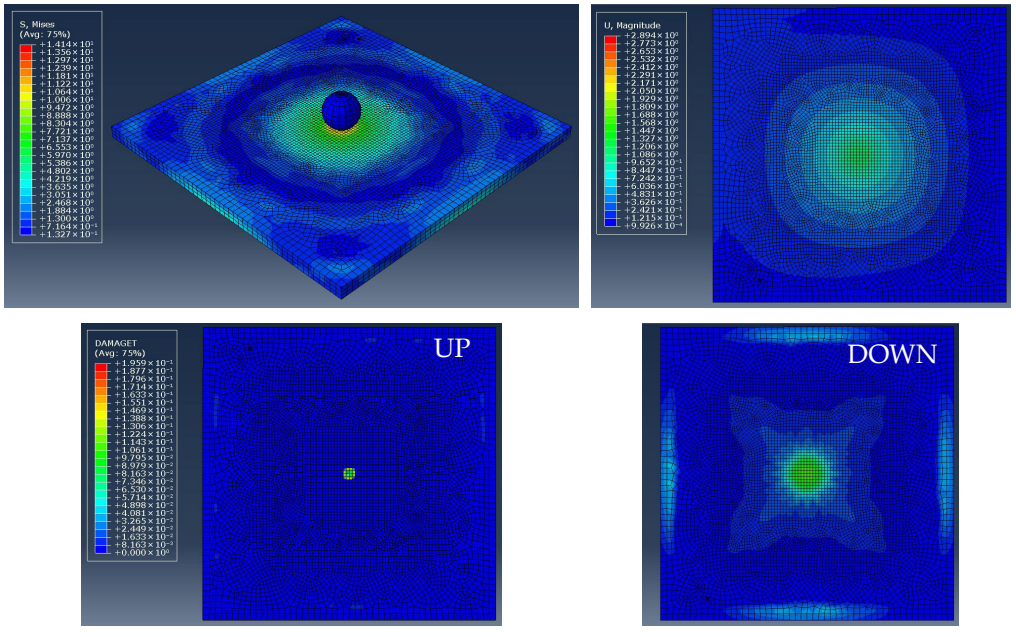
4.2. Results of FEM Analysis

The results of the numerical impact simulations are summarized in Figure 6, which reports, for each panel, the distribution of Von Mises stresses, the deflection and the tensile damage d_t of both the upper and lower surface. In particular, the results are reported at the time of maximum panel deflection, corresponding to approximately t = 0.46 s from the start of the steel ball free fall, when it reaches its lowest position and the panel deformation is at its peak. The “damaget” contour plots in Figure 6 show the distribution of the tensile damage variable d_t obtained from the CDP model. Values of d_t approaching 1 indicate fully damaged (cracked) regions, while d_t = 0 corresponds to undamaged material. A direct comparison with the experimental tests is provided in Table 6. The crack opening

width was estimated in post-processing from the maximum principal plastic strain ε^{tl} multiplied by the element size l_e (crack band approach: $w = \varepsilon^{tl} \times l_e$), consistently with the formulation adopted in the constitutive law definition (Section 4). For the UHPC panel (Figure 6a), the damage map shows a clear diagonal pattern on the lower surface, with d_5 values approaching 1 in the cracked regions. The crack opening estimated with the crack band approach is 0.45 mm, and the deflection is 4.5 mm. The UHPFRC_1 panel (Figure 6b) shows a similar damage pattern but with markedly reduced crack opening (0.24 mm) and deflection (2.8 mm). No significant damage is observed on the top surface except at the impact point. The UHPFRC_2 panel (Figure 6c) presents a different response: damage is more concentrated in the impact zone, with a crack opening of 0.28 mm and a deflection of 3.3 mm. The UHPFRC_3 panel (Figure 6d) shows a response closely aligned with UHPFRC_1, with a crack opening of 0.24 mm and deflection of 2.9 mm.

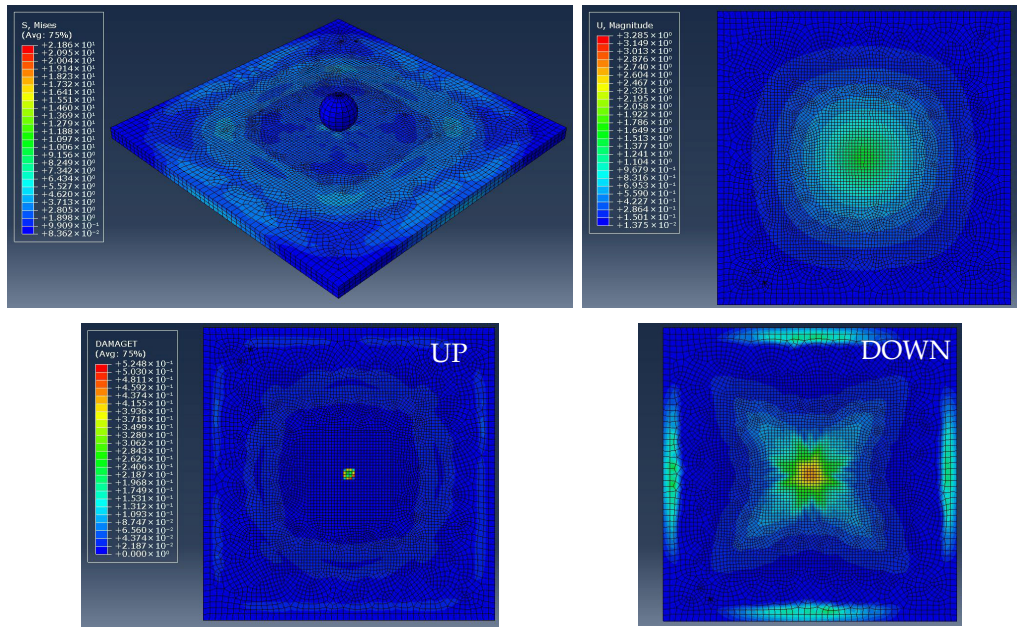


(**a**)

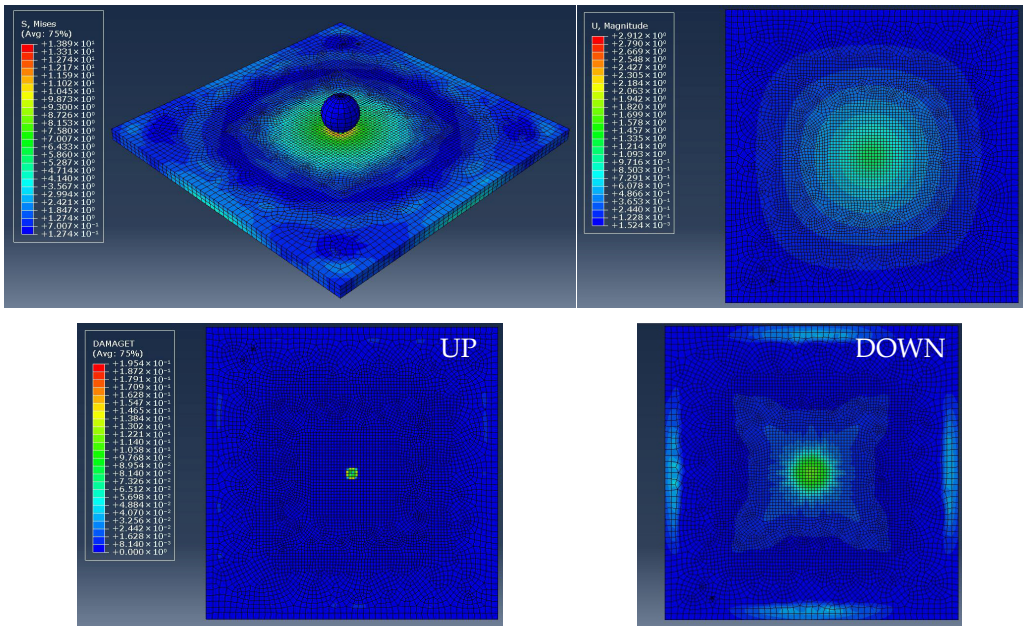


(**b**)

Figure 6. *Cont.*



(**c**)



(**d**)

Figure 6. Impact test simulation results: (**a**) plain UHPC; (**b**) UHPFRC_1; (**c**) UHPFRC_2; and (**d**) UHPFRC_3.

Table 6. Impact test results of laboratory tests and numerical simulations.

	Laboratory Tests			FEM Simulations		
Mix	**Higher Crack Opening [mm]**	**Deflection [mm]**	**Average Impact Force [kN]**	**Higher Crack Opening [mm]**	**Deflection [mm]**	**Impact Force [kN]**
UHPC	3.87	6.4	11.8	0.45	5.1	30.6
UHPFRC_1	0.19	2.4	31.5	0.24	3.5	39.1
UHPFRC_2	0.46	3.2	23.6	0.28	3.9	35.6
UHPFRC_3	0.19	2.2	34.3	0.24	3.7	37.7

Moreover, Figure 7 shows the time histories of impact force and central deflection for the four panel specimens. All panels reach maximum deflection at approximately t = 0.46 s, shortly after first contact with the steel ball. The onset of the deflection coincides with that of the impact force for all panels, consistent with the collocated measurement at the panel center. The peak impact force is lower for UHPC, equal to 30.6 kN, than for the fiber-reinforced panels, for which it ranges between 35.6 kN and 39.1 kN. This difference is consistent with the greater damage and larger deflection of the plain UHPC panel: since the average impact force is inversely related to the central deflection for the same input energy, a larger deflection corresponds to a lower force. The impact force pulse is brief and returns to zero once the steel ball separates from the panel surface. After the impact event, the panel undergoes free vibration about its deformed equilibrium position: the deflection oscillates and gradually settles to a non-zero residual value, reflecting the permanent inelastic deformation caused by cracking. The amplitude of the post-impact oscillation is larger for the plain UHPC panel, consistent with its greater damage and lower residual stiffness. The numerical results show that the hybrid mix UHPFRC_3 falls between UHPFRC_1 and UHPFRC_2, consistent with the expected behavior of a mix combining PVA microfibers and PP macrofibers.

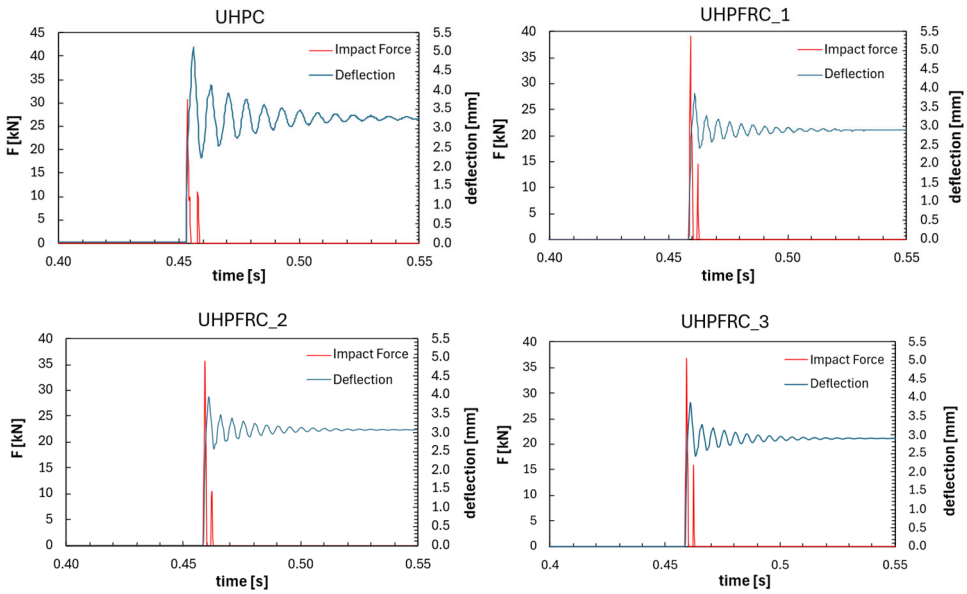


Figure 7. Time histories of impact force and central deflection.

As summarized in Table 6, the numerical results agree well with the experimental data in terms of both crack opening and deflection. The plain UHPC panel exhibits the highest values in both tests and simulations. Among the UHPFRC mixes, UHPFRC_2 shows larger crack openings and deflections than UHPFRC_1 and UHPFRC_3, consistent with the laboratory observations. The numerical model reproduces the qualitative trends of the fiber-reinforced mixes with reasonable accuracy; in particular, the hybrid mix UHPFRC_3 falls between UHPFRC_1 and UHPFRC_2 in terms of both crack opening and deflection, consistent with the expected behavior of a mix combining PVA microfibers and PP macrofibers. A significant discrepancy is observed for the plain UHPC panel: the predicted crack opening (0.45 mm) is considerably lower than the measured value (3.87 mm), attributed to the brittle, unstable fracture behavior of the unreinforced panel, which is more difficult to capture with the calibrated CDP model. The adopted inverse analysis procedure, based on EN 14651 [59] bending tests and the fib Model Code 2010 [2], proves adequate to describe the post-cracking behavior of UHPC reinforced with synthetic fibers.

These results confirm that the calibrated material model is capable of capturing the main impact-response mechanisms, including crack limitation and stiffness retention provided by synthetic fibers, and therefore represents a reliable tool for further parametric investigations.

5. Conclusions

In the present work, laboratory tests and FEM analyses were carried out on thin UHPC panels reinforced with synthetic fibers. PVA microfibers and PP macrofibers were investigated. Four panels were tested and simulated: one made of plain UHPC and three made of UHPFRC with different fiber combinations (PVA only, PP only, and hybrid PVA–PP).

Based on the results obtained, the following conclusions can be drawn:

- The mechanical characterization previously reported in [61], including three-point bending tests on notched beams, is consistent with the behavior observed under impact loading.
- Synthetic fibers significantly improve the impact resistance of thin panels without conventional bar reinforcement. Both PVA microfibers and PP macrofibers effectively reduce crack opening. PVA microfibers are particularly effective during crack initiation and early propagation stages. The use of MF 401 leads to a clear reduction in crack number and crack length.
- Fiber reinforcement also reduces deflection under impact. Panels reinforced with PVA microfibers show better overall performance compared to those reinforced only with PP macrofibers, as highlighted by the differences between UHPFRC_1 and UHPFRC_2.
- The numerical simulations reproduce both the trends and the magnitude of the experimental results. The plain UHPC panel exhibits the largest crack openings and deflections, while all fiber-reinforced panels show improved behavior. Among them, UHPFRC_2 consistently presents larger crack openings compared to UHPFRC_1 and UHPFRC_3.

Future research will focus on improving the modeling of high- and ultra-high-performance concretes reinforced with synthetic fibers. In particular, further refinement of the inverse analysis procedure is required to define constitutive models capable of accurately describing the toughness and post-cracking response of ultra-high-strength concretes with synthetic fibers. The inverse analysis approach proposed in the fib Model Code 2010 was primarily developed for steel fiber-reinforced concrete and may not fully capture the crack-bridging mechanisms typical of synthetic fibers. The development and calibration of dedicated models for synthetic fiber reinforcement are therefore necessary for reliable numerical simulations and design applications.

Additional experimental investigations on impact behavior are also needed. Future tests should consider different fiber contents and varying impact energy levels in order to better quantify damage evolution, crack propagation, and energy absorption capacity under dynamic loading.

Author Contributions: Conceptualization, F.M. and M.A.A.; methodology, F.M. and P.S.R.; formal analysis, V.R.; resources, S.M.; data curation, V.R.; writing—original draft preparation, V.R.; writing—review and editing, F.M., P.S.R. and S.M.; and supervision, M.A.A. All authors have read and agreed to the published version of the manuscript.

Funding: This research received no external funding.

Data Availability Statement: The original contributions presented in this study are included in the article. Further inquiries can be directed to the corresponding author.

Conflicts of Interest: Author Sandro Moro was employed by the company Master Builders Solutions. The remaining authors declare that the research was conducted in the absence of any commercial or financial relationships that could be construed as a potential conflict of interest.

References

1. *ASTM C1856/C1856M*; Standard Practice for Fabricating and Testing Specimens of Ultra-High Performance Concrete. ASTM: West Conshohocken, PA, USA, 2017.
2. CEB-FIP. *Fib Model Code for Concrete Structures*; John Wiley & Sons: Hoboken, NJ, USA, 2010. [CrossRef]
3. *EN 1992-1-1*; Eurocode 2: Design of Concrete Structures—Part 1-1: General Rules and Rules for Buildings. British Standard Institution: London, UK, 2004.
4. Yi, F.; Kazmi, S.M.S.; Hu, B.; Wu, Y.-F. Mitigating the brittle behavior of compression cast concrete using polypropylene fibers. *Constr. Build. Mater.* **2024**, *440*, 137435. [CrossRef]
5. Yoo, D.Y.; Banthia, N. Impact resistance of fiber-reinforced concrete—A review. *Cem. Concr. Compos.* **2019**, *104*, 103389. [CrossRef]
6. Yoo, D.-Y.; Gohil, U.; Gries, T.; Yoon, Y.-S. Comparative low-velocity impact response of textile-reinforced concrete and steel-fiber-reinforced concrete beams. *J. Compos. Mater.* **2016**, *50*, 2421–2431. [CrossRef]
7. Yoo, D.-Y.; Yoon, Y.-S. Influence of steel fibers and fiber-reinforced polymers on the impact resistance of one-way concrete slabs. *J. Compos. Mater.* **2014**, *48*, 695–706. [CrossRef]
8. Ren, B.; Ma, G.; Wu, J.; Chang, R.; Hu, R. Stress-wave propagation and wave-induced damage patterns of filter concrete under blast loading. *J. Build. Eng.* **2026**, *119*, 115295. [CrossRef]
9. Bentur, A.; Mindess, S. *Fibre Reinforced Cementitious Composites*; CRC Press: Boca Raton, FL, USA, 2006. [CrossRef]
10. *ACI 544.4R-18*; Guide for Design with Fiber-Reinforced Concrete. ACI: Farmington Hills, MI, USA, 2018.
11. Pakravan, H.R.; Ozbakkaloglu, T. Synthetic fibers for cementitious composites: A critical and in-depth review of recent advances. *Constr. Build. Mater.* **2019**, *207*, 491–518. [CrossRef]
12. Ramezanianpour, A.A.; Esmaeili, M.; Ghahari, S.A.; Najafi, M.H. Laboratory study on the effect of polypropylene fiber on durability, and physical and mechanical characteristic of concrete for application in sleepers. *Constr. Build. Mater.* **2013**, *44*, 411–418. [CrossRef]
13. Ahmed, S.F.U.; Mihashi, H. A review on durability properties of strain hardening fibre reinforced cementitious composites (SHFRCC). *Cem. Concr. Compos.* **2007**, *29*, 365–376. [CrossRef]
14. Zhang, B.; Lin, X.; Zhang, Y.X.; Zhang, L. Microscale failure analysis of the ultra-high-performance polypropylene fibre reinforced concrete panel subjected to high thermal loading induced by fire exposure. *Eng. Struct.* **2023**, *292*, 116518. [CrossRef]
15. Kalifa, P.; Chéné, G.; Gallé, C. High-temperature behaviour of HPC with polypropylene fibres. *Cem. Concr. Res.* **2001**, *31*, 1487–1499. [CrossRef]
16. Serrano, R.; Cobo, A.; Prieto, M.I.; de las Nieves González, M. Analysis of fire resistance of concrete with polypropylene or steel fibers. *Constr. Build. Mater.* **2016**, *122*, 302–309. [CrossRef]
17. Ríos, J.D.; Leiva, C.; Ariza, M.P.; Seitl, S.; Cifuentes, H. Analysis of the tensile fracture properties of ultra-high-strength fiber-reinforced concrete with different types of steel fibers by X-ray tomography. *Mater. Des.* **2019**, *165*, 107582. [CrossRef]
18. Zhang, S.; Zhang, C.; Liao, L. Investigation on the relationship between the steel fibre distribution and the post-cracking behaviour of SFRC. *Constr. Build. Mater.* **2019**, *200*, 539–550. [CrossRef]
19. Marcos-Meson, V.; Solgaard, A.; Fischer, G.; Edvardsen, C.; Michel, A. Pull-out behaviour of hooked-end steel fibres in cracked concrete exposed to wet-dry cycles of chlorides and carbon dioxide—Mechanical performance. *Constr. Build. Mater.* **2020**, *240*, 117764. [CrossRef]
20. Yang, L.; Zhang, Z.; Gao, D.; Tang, J.; Chang, H.; Liu, G. Mechanical property evolution and chloride transport of steel fiber-reinforced concrete exposed to simulated marine environments. *Mater. Struct.* **2022**, *55*, 130. [CrossRef]
21. Chen, G.; Hadi, M.N.S.; Gao, D.; Zhao, L. Experimental study on the properties of corroded steel fibres. *Constr. Build. Mater.* **2015**, *79*, 165–172. [CrossRef]
22. Söylev, T.A.; Özturan, T. Durability, physical and mechanical properties of fiber-reinforced concretes at low-volume fraction. *Constr. Build. Mater.* **2014**, *73*, 67–75. [CrossRef]
23. Anandan, S.; Manoharan, S.V.; Sengottian, T. Corrosion Effects on the Strength Properties of Steel Fibre Reinforced Concrete Containing Slag and Corrosion Inhibitor. *Int. J. Corros.* **2014**, *2014*, 595040. [CrossRef]
24. Guerini, V.; Conforti, A.; Plizzari, G.; Kawashima, S. Influence of steel and macro-synthetic fibers on concrete properties. *Fibers* **2018**, *6*, 47. [CrossRef]
25. Yin, S.; Tuladhar, R.; Shi, F.; Combe, M.; Collister, T.; Sivakugan, N. Use of macro plastic fibres in concrete: A review. *Constr. Build. Mater.* **2015**, *93*, 180–188. [CrossRef]
26. Ahmad, J.; Zhou, Z. Mechanical Properties of Natural as well as Synthetic Fiber Reinforced Concrete: A Review. *Constr. Build. Mater.* **2022**, *333*, 127353. [CrossRef]

27. Pakravan, H.R.; Memariyan, F. Modification of low-surface energy fibers used as reinforcement in cementitious composites: A review. *Polym.-Plast. Technol. Eng.* **2017**, *56*, 227–239. [CrossRef]
28. Won, J.P.; Lim, D.H.; Park, C.G. Bond behaviour and flexural performance of structural synthetic fibre-reinforced concrete. *Mag. Concr. Res.* **2006**, *58*, 401–410. [CrossRef]
29. Oh, B.H.; Kim, J.C.; Choi, Y.C. Fracture behavior of concrete members reinforced with structural synthetic fibers. *Eng. Fract. Mech.* **2007**, *74*, 243–257. [CrossRef]
30. Behfarnia, K.; Behravan, A. Application of high performance polypropylene fibers in concrete lining of water tunnels. *Mater. Des.* **2014**, *55*, 274–279. [CrossRef]
31. Aslani, F.; Nejadi, S. Self-compacting concrete incorporating steel and polypropylene fibers: Compressive and tensile strengths, moduli of elasticity and rupture, compressive stress–strain curve, and energy dissipated under compression. *Compos. B Eng.* **2013**, *53*, 121–133. [CrossRef]
32. Sun, Z.; Xu, Q. Microscopic, physical and mechanical analysis of polypropylene fiber reinforced concrete. *Mater. Sci. Eng. A* **2009**, *527*, 198–204. [CrossRef]
33. Medina, N.F.; Barluenga, G.; Hernández-Olivares, F. Enhancement of durability of concrete composites containing natural pozzolans blended cement through the use of Polypropylene fibers. *Compos. B Eng.* **2018**, *61*, 214–221. [CrossRef]
34. Sadrinejad, I.; Madandoust, R.; Ranjbar, M.M. The mechanical and durability properties of concrete containing hybrid synthetic fibers. *Constr. Build. Mater.* **2018**, *178*, 72–82. [CrossRef]
35. Kim, D.J.; Wille, K.; El-Tawil, S.; Naaman, A.E. Testing of Cementitious Materials under High-Strain-Rate Tensile Loading Using Elastic Strain Energy. *J. Eng. Mech.* **2011**, *137*, 268–275. [CrossRef]
36. Gupta, P.; Banthia, N.; Yan, C. Fiber Reinforced Wet-Mix Shotcrete under Impact. *J. Mater. Civ. Eng.* **2000**, *12*, 81–90. [CrossRef]
37. Murali, G.; Wong, L.S.; Abid, S.R. A comprehensive review of drop weight impact testing: Evaluating the Pros and Cons in fiber-reinforced concrete performance assessment. *J. Build. Eng.* **2024**, *94*, 109934. [CrossRef]
38. Grote, D.L.; Park, S.W.; Zhou, M. Dynamic behavior of concrete at high strain rates and pressures: I. experimental characterization. *Int. J. Impact Eng.* **2001**, *25*, 869–886. [CrossRef]
39. Feng, J.; Gao, X.; Li, J.; Dong, H.; He, Q.; Liang, J.; Sun, W. Penetration resistance of hybrid-fiber-reinforced high-strength concrete under projectile multi-impact. *Constr. Build. Mater.* **2019**, *202*, 341–352. [CrossRef]
40. Kim, D.J.; El-Tawil, S.; Naaman, A.E. Rate-dependent tensile behavior of high performance fiber reinforced cementitious composites. *Mater. Struct.* **2009**, *42*, 399–414. [CrossRef]
41. Abid, S.R.; Murali, G.; Ahmad, J.; Al-Ghasham, T.S.; Vatin, N.I. Repeated Drop-Weight Impact Testing of Fibrous Concrete: State-Of-The-Art Literature Review, Analysis of Results Variation and Test Improvement Suggestions. *Materials* **2022**, *15*, 3948. [CrossRef]
42. Jacobsen, Ø.E.K.; Kristoffersen, M.; Dey, S.; Børvik, T. Projectile Impact on Plain and Reinforced Concrete Slabs. *J. Dyn. Behav. Mater.* **2024**, *10*, 137–159. [CrossRef]
43. Guan, Z.; Li, Y.; Lai, Z.; Zhou, H.; Qin, J.; Wen, Y.; Chen, Y.; Huang, R. Size effect of concrete based on split Hopkinson pressure bar (SHPB) test. *Constr. Build. Mater.* **2024**, *441*, 137499. [CrossRef]
44. Zhou, Y.; Yang, J.; Luo, X.; Hwang, H.J.; Chen, H.; Sun, J.; Yi, W.; Kang, S.M. Pendulum impact loading tests of precast concrete columns with various column base connections. *Eng. Struct.* **2022**, *252*, 113736. [CrossRef]
45. Bentur, A.; Mindess, S.; Banthia, N. The behaviour of concrete under impact loading: Experimental procedures and method of analysis. *Mater. Struct.* **1986**, *19*, 371–378. [CrossRef]
46. Murali, G.; Haridharan, M.K.; Abid, S.R.; Mohan, C.; Khera, G.S.; Bandhavi, C. Compressive strength and impact strength of preplaced aggregate fibre reinforced concrete. *Mater. Today Proc.* **2023**, *In press*. [CrossRef]
47. Zhang, Q.; Yuan, R.; Wang, D.; Feng, C.; Yue, J.; Sun, L. The impact fracture characteristics of concrete slabs under different hammerhead shapes, impact velocities and concrete strengths. *Constr. Build. Mater.* **2023**, *392*, 131919. [CrossRef]
48. Mohammed, A.A.; Karim, S.H. Impact strength and mechanical properties of high strength concrete containing PET waste fiber. *J. Build. Eng.* **2023**, *68*, 106195. [CrossRef]
49. El-Abbasy, A.A. Tensile, flexural, impact strength, and fracture properties of ultra-high-performance fiber-reinforced concrete—A compre-hensive review. *Constr. Build. Mater.* **2023**, *408*, 133621. [CrossRef]
50. He, H.; Wu, L.; Zhi, X.; Fan, F.; Ma, G.; Zhang, R. Dynamic responses and failure modes of ultra-high strength alkali-activated concrete slab under impact load. *Eng. Struct.* **2026**, *353*, 122258. [CrossRef]
51. Körmeling, H.A.; Reinhardt, H.W. Strain rate effects on steel fibre concrete in uniaxial tension. *Int. J. Cem. Compos. Lightweight Concr.* **1987**, *9*, 197–204. [CrossRef]
52. Fujikake, K.; Senga, T.; Ueda, N.; Ohno, T.; Katagiri, M. Effects of Strain Rate on Tensile Behavior of Reactive Powder Concrete. *J. Adv. Concr. Technol.* **2006**, *4*, 79–84. [CrossRef]

53. Wille, K.; El-Tawil, S.; Naaman, A.E. Strain Rate Dependent Tensile Behavior of Ultra-High Performance Fiber Reinforced Concrete. In *High Performance Fiber Reinforced Cement Composites*; Springer: Berlin/Heidelberg, Germany, 2012; pp. 381–387. [CrossRef]
54. Pyo, S.; Wille, K.; El-Tawil, S.; Naaman, A.E. Strain rate dependent properties of ultra high performance fiber reinforced concrete (UHP-FRC) under tension. *Cem. Concr. Compos.* **2015**, *56*, 15–24. [CrossRef]
55. Bindiganavile, V.; Banthia, N. Generating dynamic crack growth resistance curves for fiber-reinforced concrete. *Exp. Mech.* **2005**, *45*, 112–122. [CrossRef]
56. Suaris, W.; Shah, S.P.; Asce, M. Properties of concrete subjected to impact. *J. Struct. Eng.* **1983**, *109*, 1727–1741. [CrossRef]
57. Bindiganavile, V.; Banthia, N. Polymer and Steel Fiber-Reinforced Cementitious Composites under Impact Loading—Part 2: Flexural Toughness. *ACI Mater. J.* **2001**, *98*, 17–24.
58. Bindiganavile, V.; Banthia, N.; Aarup, B. Impact Response of Ultra-High-Strength Fiber-Reinforced Cement Composite. *ACI Mater. J.* **2002**, *99*, 543–548.
59. *UNI EN 14651*; Test Method for Metallic Fibered Concrete—Measuring the Flexural Tensile Strength. European Committee for Standardization: Brussels, Belgium, 2005.
60. *ASTM C1609/C 1609M—07*; Standard Test Method for Flexural Performance of Fiber-Reinforced Concrete (Using Beam with Third-Point Loading). ASTM: West Conshohocken, PA, USA, 2009.
61. Romanazzi, V.; Micelli, F.; Moro, S.; Ros, P.S.; Aiello, M.A. Experimental characterization of VHPC reinforced with short synthetic fibers. *Mater. Struct.* **2025**, *58*, 82. [CrossRef]
62. Blasi, G.; Leone, M. Inverse analysis-based model for the tensile behaviour of fibre-reinforced concrete with manufactured and waste tyres recovered fibres. *Case Stud. Constr. Mater.* **2022**, *17*, e01297. [CrossRef]
63. Fakeh, M.; Jawdhari, A.; Fam, A. Recommended concrete damage plasticity parameters and constitutive models for UHPC in ABAQUS. *Eng. Struct.* **2025**, *333*, 120154. [CrossRef]
64. Wang, Z.; Yan, J.; Lin, Y.; Fan, F. Influence of shear connectors on the ultimate capacity of steel-UHPC-steel slabs subjected to concentrated loads. *Eng. Struct.* **2021**, *231*, 111763. [CrossRef]
65. Romanazzi, V.; Micelli, F.; Moro, S.; Aiello, A.; Kandalaft, A.G. Very High-Performance Fiber Reinforced Concrete (VHPFRC) Testing and Finite Element Analysis. In Proceedings of the Recent Advances in Concrete Technology and Sustainability Issues—Conference Proceedings SP-355, Milan, Italy, 13–15 July 2022.

Disclaimer/Publisher's Note: The statements, opinions and data contained in all publications are solely those of the individual author(s) and contributor(s) and not of MDPI and/or the editor(s). MDPI and/or the editor(s) disclaim responsibility for any injury to people or property resulting from any ideas, methods, instructions or products referred to in the content.